

2016 April 8

## A Wide-Field Camera and Fully Remote Operations at the Wyoming Infrared Observatory

Joseph R. Findlay<sup>1</sup>, Henry A. Kobulnicky<sup>1</sup>, James S. Weger<sup>1</sup>, Gerald A. Bucher<sup>1</sup>,  
Marvin C. Perry<sup>1</sup>, Adam D. Myers<sup>1</sup>, Michael J. Pierce<sup>1</sup>, Conrad Vogel<sup>2</sup>

joseph.findlay@uwyo.edu

### ABSTRACT

Upgrades at the 2.3 meter Wyoming Infrared Observatory telescope have provided the capability for fully-remote operations by a single operator from the University of Wyoming campus. A line-of-sight 300 Megabit s<sup>-1</sup> 11 GHz radio link provides high-speed internet for data transfer and remote operations that include several real-time video feeds. Uninterruptable power is ensured by a 10 kVA battery supply for critical systems and a 55 kW autostart diesel generator capable of running the entire observatory for up to a week. Construction of a new four-element prime-focus corrector with fused-silica elements allows imaging over a 40' field-of-view with a new 4096<sup>2</sup> UV-sensitive prime-focus camera and filter wheel. A new telescope control system facilitates the remote operations model and provides 20'' rms pointing over the usable sky. Taken together, these improvements pave the way for a new generation of sky surveys supporting space-based missions and flexible-cadence observations advancing emerging astrophysical priorities such as planet detection, quasar variability, and long-term time-domain campaigns.

*Subject headings:* instrumentation: miscellaneous — instrumentation: photometers — telescopes

---

<sup>1</sup>Department of Physics & Astronomy, University of Wyoming, Laramie, WY 82070, USA

<sup>2</sup>Steward Observatory, University of Arizona, Tucson, AZ 85721, USA

## 1. Introduction

The Wyoming Infrared Observatory (WIRO) 2.3-meter classical Cassegrain telescope was constructed by the University of Wyoming in 1977 as (briefly) the world’s largest infrared-optimized telescope and the first fully computer-controlled telescope (Gehrz & Hackwell 1978). Situated at 9656 feet (2935 m) above sea level atop Mt. Jelm, 25 miles southwest of Laramie, WY, it is one of the highest research observatories in the continental U.S. WIRO remains one of the largest telescopes that is 100% operated by a single institution. The equatorial yoke-mounted telescope has an f/27 Cassegrain focus (with optional chopping secondary) and an f/2.1 prime focus, providing plate scales of  $3''.32 \text{ mm}^{-1}$  and  $43'' \text{ mm}^{-1}$ , respectively. Among its achievements, it performed early infrared observations of dust in evolved stars, (Hackwell et al. 1979; Gehrz et al. 1980) and some of the first maps of infrared sources (Gehrz et al. 1982; Hackwell et al. 1982). More recently it has been used to map the star formation rates in the local universe (Dale et al. 2010) and complete a statistical census of orbital parameters in a large sample of massive binary stars (Kobulnicky et al. 2014). WIRO has enabled hands-on telescope and instrumentation training for generations of graduate and undergraduate students while contributing to over 45 doctoral dissertations and over 115 refereed journal articles.<sup>1</sup>

A series of recent upgrades to the telescope and instrument suite have equipped WIRO for a new generation of large-scale surveys and synoptic programs. Section 2 introduces the new control system installed in November of 2008, replacing the 1980’s-era telescope electronics and control loop software. Section 3 describes a new prime-focus corrector built and implemented in 2004. Section 4 details a new prime-focus assembly and CCD camera implemented in 2014. Section 5 highlights infrastructure allowing fully-remote single-operator observations from the University of Wyoming campus. Together, these improvements have allowed more efficient and effective use of this small- mid-sized telescope.

## 2. Telescope Control System

In 2008 General Dynamics (GD) SATCOM, Inc. designed and built a control system, in consultation with WIRO staff, for the 2.3 meter telescope and dome. It was installed in November 2008 by GD SATCOM and WIRO staff as the most significant upgrade of the telescope infrastructure since its construction. Encoders on the R.A. and Dec. axes are located on worm gears that drive the bull gears on each axis at a rate of  $0.5^\circ$  per rotation

---

<sup>1</sup>The WIRO website at <http://physics.uwyo.edu/~WIRO> maintains a list publications.

of the worm gear. The old encoders (14-bits per turn) were replaced with 37-bit (25-bits per turn plus 12 bits to encode absolute position) Heidenhain ROQ437 multiturn encoders. The original drive motors and pre-load motors<sup>2</sup> were retained. A Clifton Precision synchro-brushless resolver model 11-BHW<sup>3</sup> mounted on the rotating dome ring reports dome azimuth to 0.1 degrees.

Amplifiers for telescope and dome motors reside in a custom chassis, provided by GD SATCOM, located in the WIRO control room. The chassis contains pulse width modulation servo motor amplifiers, an Advanced Motion Controls model 25A8<sup>4</sup> for low-level velocity loop control of R.A. and Dec., and a central control unit (CCU) for position loop control of each axis. Communications between the CCU and telescope control computer, located in an adjacent rack and running real time linux (QNX), occurs over a short RS422 connection. A six-parameter pointing model within the GD SATCOM control loop applies differential corrections for small misalignment of each of the telescope axes in each of two dimensions, including a term for zero points of each axis. Dome azimuth is synchronized to telescope location under normal sidereal tracking modes, with a deadband of three degrees to inhibit constant dome motion while preventing occultation.

Operators control the telescope from a linux PC serving as the front end to the GD SATCOM telescope control computer. The text-driven front-end C code is derived from the previous WIRO telescope control system developed at UW (Spillar et al. 1993), which, in turn, has roots in the 1976-era FORTH control code originally implemented at WIRO. The front-end C code passes telescope and dome commands to the telescope control computer and reads telescope status from the telescope control computer using formatted text strings over ethernet. The front-end interface allows arbitrary R.A. & Dec. offsets, which are stored upon shutdown, and implements a capability for non-sidereal tracking inherent in the SATCOM control loop; users may specify non-sidereal rates in R.A. and Dec. in arc-seconds per second.

Telescope pointing is  $\approx 20''$  RMS over the sky at zenith angles less than  $60^\circ$ . Open-loop exposures of up to five minutes are routinely obtained with negligible tracking error.

---

<sup>2</sup>Drive motors on each axis are Inland Torque model T-7202-E with Inland Tachometer Generator model TD-5110-B tachometers for rate control loop feedback. Tachometers are mounted on the same shaft as the torque motors. Pre-load motors are Inland Torque Motor model T-7203-C. Inland Torque is now part of Kollmorgen and these parts are no longer in production. The interested reader should contact Kollmorgen for advice on equivalent products.

<sup>3</sup>Clifton Precision is now part of MOOG.

<sup>4</sup>This product is no longer available to new applications, contact Advanced Motion Controls to identify an equivalent.

Maximum slew rates are 40 degrees per minute on each axis. Settle times are about eight seconds. The encoders and control system electronics have proven robust against lightning during summer storms. An extensive system of grounding and surge suppression (Section 5) has also helped to minimize electrical damage.

### 3. A New Wide-Field Prime-Focus Corrector

The 2.3-meter primary mirror of WIRO is an f/2.1 paraboloid and, as such, it suffers from off-axis coma that severely limits its usable field of view. In the late 1980's Ed Loh and Earl Spillar designed a four-element prime focus corrector for WIRO based upon the designs of Wynne (1965, 1973) that provided a usable field of about 8'. Since that time, much larger format CCD detectors have become available. In 2003 we undertook the design of a new prime-focus camera and wide-field corrector in order to provide WIRO with a modern, survey imaging capability. The new four-element corrector was designed to produce sub-arcsecond images over the 40' field that the latest 4096 × 4096 CCDs would cover. UV-grade fused silica (Corning 7980 HPFS) was chosen for the corrector material in order to allow its use from the atmospheric cutoff at ~ 310 nm to the long-wavelength limit for silicon detectors, ~ 1000 nm. The corrector design was developed by Charles Harmer (NOAO) with the assistance of one of us (HAK) using the ZEMAX optical design program. The RMS spot radius at wavelengths of 0.37, 0.55, and 1.0 μm was minimized over fields of 0, 7, 14, 17, and 20' along the X-Y diagonal. A back focal distance of >70 mm from the rear element was maintained in order to allow mechanical clearance for a 12 mm thick filter wheel, the mechanical focusing stage, and for the Dewar window to safely clear the detector.

Figure 1 shows a schematic view of the corrector with each of its eight spherical surfaces (A1, A2, B1, ..., etc.) labeled. Table 1 lists the prescription of each element. Each lens surface (column 1) entails a clear diameter (column 2), a thickness and separation at center (column 3), and a radius of curvature (column 4). Tolerances are 0.1% on each radius of curvature, 0.1 mm in thickness, and <20 μm of thickness difference between the two surfaces (wedge). The glass mass of all four elements is 3.0 kg. Thermal analysis between 20°C and -20°C indicated that aluminum was a suitable material for the lens mounts and the entire optomechanical structure.

Figure 2 shows a spot diagram illustrating the designed optical performance of the corrector at 0.37 μm wavelength at field angles of 0', 5', 10', 12', 14', and 19' along the X-Y diagonal. The box is 50 μm square, corresponding to approximately 2''4 on the sky, or about 4 pixels for a 15 μm pixel size. The resulting spot sizes are significantly smaller than 1'' in all but the largest field angles. The predicted 120 μm focus shift between wavelengths

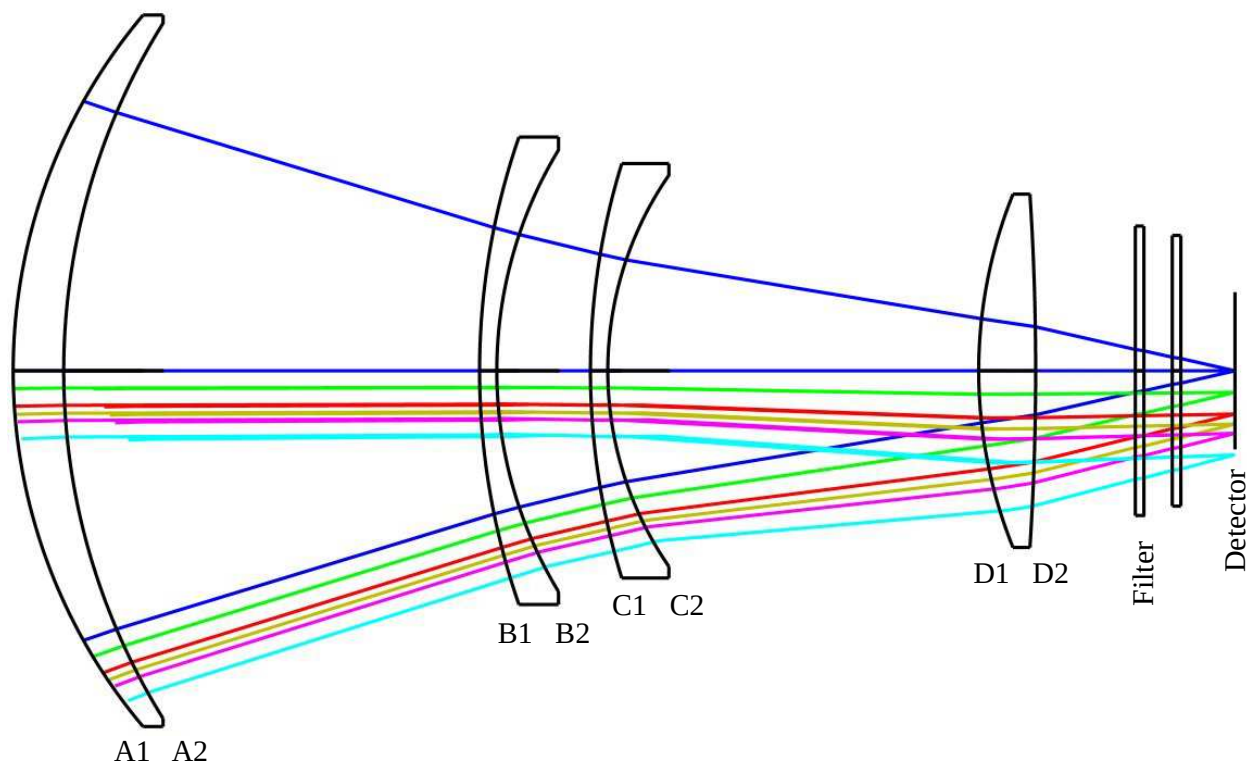


Fig. 1.— Schematic design of the four-element prime-focus corrector constructed for use on the WIRO telescope. The diameter of the largest element is 250 mm. Labels correspond to the rows of Table 1, which give the prescription for each surface.

Table 1. Optical Prescription for the four-element WIRO Prime-Focus Corrector

Surface	Diameter (mm)	Thickness (mm)	$R_{curve}$ (mm)
A1	249.6	17.92	193.67
A2	243.8	145.20	230.86
B1	164.4	6.00	250.40
B2	155.2	33.71	149.53
C1	145.4	6.00	245.90
C2	137.4	130.10	120.65
D1	124.0	20.00	165.67
D2	122.0	...	-949.12

of  $0.37\ \mu\text{m}$  and  $1\ \mu\text{m}$  has proven undetectable during routine operation. The distortion over the flat focal plane is less than 2%. The individual lens elements were manufactured by Harold Johnson Optical Laboratories, Inc. and coated with a single layer  $\text{MgF}_2$  anti-reflection coating optimized for  $550\ \text{nm}$ .

The mechanical design of the corrector was subcontracted to the Pilot Group of Monrovia, CA. Their design consists of individual lens cells assembled and pinned into a stack to complete the corrector assembly. The design includes a system of thin, internal rings for stray light baffling. The completed stack of lens cells squeeze thin rubber gaskets between each cell to seal the entire assembly so that it can be filled with dry  $\text{N}_2$  in order to minimize internal condensation. The individual mechanical components were manufactured by Wyoming's Division of Research Support and flat black anodized in order to minimize internal reflections.

The assembly and alignment process was done by one of us (MP) on a precision turntable via laser illumination of each lens within its cell. Design specifications called for  $<1'$  tilt on each element, centering of the elements to within  $<0.1\ \text{mm}$ , and relative spacing of the elements to within  $0.1\ \text{mm}$ . The procedure for aligning the lenses within their cells to ensure the optical axes correspond with the mechanical axis of the assembly is as follows; each lens cell was placed upon the turntable, mechanically centered via a dial indicator and clamped in place. The lens was then placed upon its reference surface within its oversized mount and the reflected laser beam examined with a microscope as the turntable was rotated. The laser does not need to be aligned with the rotational axis during this process. If the optical axis of the lens is aligned with the mechanical axis its beam will be reflected from a point at constant radius, and hence constant slope, as the lens cell is rotated. Thus the reflected beam does not move as the assembly is rotated. However if the optical axis of the lens is displaced from the mechanical axis a rotation of the assembly results in the beam reflecting off of a surface of changing slope and the beam will wobble as the assembly is rotated. The lens is adjusted until the wobble is removed at which point it reflects from a constant slope and radius meaning that the optical axis of the lens is now coincident with the mechanical axis of the assembly.

The position of the lens element was adjusted using four nylon radial setscrews until the beam was stationary indicating that the optical axis of the lens was aligned with the rotational (mechanical) axis of its lens mount. Space grade silicone RTV (Dow Corning 93-500) was mixed with hardener and placed within a vacuum chamber in order to remove air bubbles. The RTV was then drawn with a large-gauge hypodermic needle and extruded into the gap between the lens and its cell. When the RTV had set, the adjustment screws were withdrawn and the holes filled with RTV. The lens and its mount were then set aside

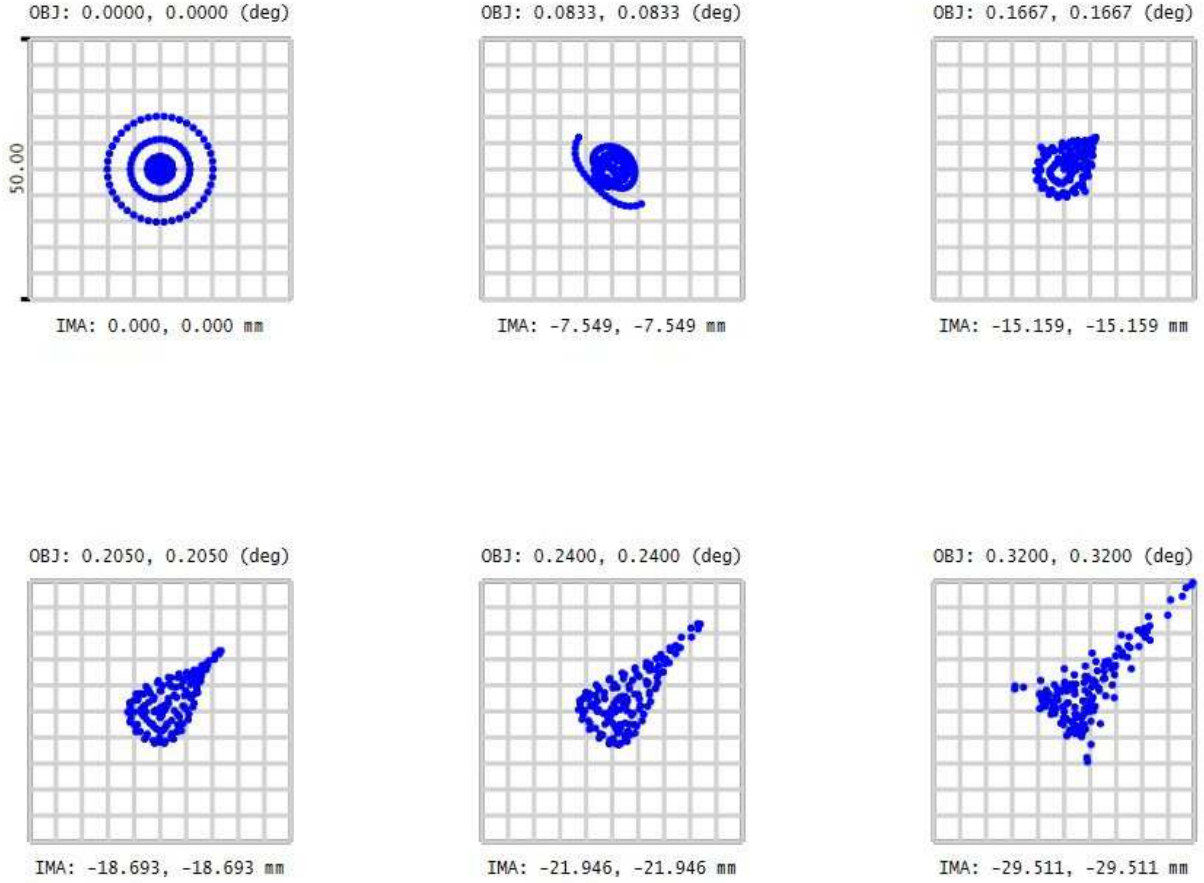


Fig. 2.— Spot diagram illustrating imaging performance of the WIRO prime-focus corrector as a function of field angle at  $0.37 \mu\text{m}$  wavelength. Each box is  $50 \mu\text{m}$  square, corresponding to approximately  $2''.4$  on the sky. Field angles of  $0'$ ,  $5'$ ,  $10'$ ,  $12'$ ,  $14'$ , and  $19'$  along the X-Y diagonal are shown.

and the process repeated for the next lens and mount. The corrector stack was assembled using alignment pins and screws to hold the individual lens cells and baffles in place while compressing a gasket between each pair of cells. The completed corrector assembly was then pumped free of air and filled with dry  $N_2$ . Afterward, the ports were filled with RTV.

The corrector was then shipped to WIRO for incorporation within the prime focus camera assembly. The prime-focus instrument package is mounted on a large stage within a box supported by a four-vane spider of the prime-focus ring. The two axial stages allow independent motion of the corrector and the detector. The horizontal instrument stage allows the prime-focus assembly to be mechanically centered within the prime-focus ring of the telescope.<sup>5</sup> The corrector was aligned with the optical axis of WIRO over a period of several nights. First, the optical axis of the telescope primary was identified by imaging star fields without the corrector in place. The size of the strongly comatic star images were measured and the center of the pattern computed. The primary mirror was then aligned to bring its optical axis to the center of the detector. The corrector installed at its nominal axial position relative to the detector. Images taken inside and outside of focus were used to determine the position of best focus across the field and the detector tilt computed. Shims were used to ensure that the detector mounted perpendicular to the optical axis. Additional images were used to determine the optimal radial and axial location of the corrector, at which point the corrector was judged to be aligned. The point-spread-function of the images across a  $13'$  field of view were found to suffer from approximately  $0.1''$  of astigmatism, but rotation of the corrector resulted in no change of the position angle, implying that the astigmatism is present in WIRO's primary mirror. On the best nights at WIRO the resulting images have  $\text{FWHM} \simeq 1.0''$ .

#### 4. The WIRO Double-Prime Instrument Package

In 2014 a new prime-focus instrument package was implemented at WIRO to take full advantage of the field of view offered by the prime-focus corrector. A new focus stage and filter wheel were constructed in the University of Wyoming Division of Research Support shops. A new 4k CCD camera was purchased to enable wide-field imaging over the  $\sim 40'$

---

<sup>5</sup>The corrector was originally installed and tested with the previous-generation prime-focus imager, known as WIRO Prime, designed and built by MP. WIRO Prime was in operation for approximately 10 years, 2004–2013. WIRO prime consisted of two stages mounted on shafts using linear bearings. Stepper motors turned precision screws to position the stages along WIRO's optical axis. A twelve slot filter wheel holding two-inch filters and the corrector were mounted to one of the stages and an Astrophysical Research Camera ND-5 Dewar containing a  $2048 \times 2048$  E2V CCD detector on the other.

field provided by the corrector. Dubbed “WIRO Double-Prime” to signify the roughly 100% increase in field of view relative to the old prime-focus assembly and 2k CCD camera, it was constructed during 2013–2014 and commissioned during the summer and fall of 2014.

#### 4.1. Focus and Filter Wheel Mechanisms

Figure 3 displays a labeled photograph of the WIRO Double Prime prime-focus assembly. It is an upgraded version of that used in WIRO Prime and it consists of a circular aluminum base plate that mounts to the telescope’s prime-focus interface box and a traveling plate that supports the filter wheel, CCD Dewar, position sensor, and motors that drive the filter wheel and focus. The traveling plate translates along the optical axis via two parallel stainless steel rails driven by two Ultramotion D1 linear actuators acting against a spring that supplies tension to couple the traveling plate to the base plate. The actuators are coupled in software to ensure simultaneous motion. The distance between the base plate and traveling plate is encoded to within  $\sim 1 \mu\text{m}$  rms by a Keyence GT2 Digital Contact Sensor. The traveling plate supports a five-position filter wheel that can accept filters up to 3.25 inches square; smaller filters may be used with the addition of custom insets, at the cost of reduced field of view. A pneumatic piston driven by a 45 p.s.i. dry nitrogen supply hose locks the wheel at one of the five filter positions defined by the location of conical detents machined into the periphery of the filter wheel. This passive mechanical torque obviates the need for the Applied Motion Products Inc. high-torque NEMA size 23 stepper motor to supply holding torque on the filter wheel and ensures precise filter positioning. A Pepperl+Fuchs AHS58-H absolute single-turn encoder with 16-bit resolution located on the shaft of the filter wheel motor monitors filter wheel rotation to  $0.33'$ . A Dewar containing the CCD mounts at the location of the cover plate pictured in Figure 3. The Uniblitz<sup>6</sup> model CS90HS1T0 iris type shutter, driven by a Uniblitz model VCM-D1 driver, resides just behind the cover plate. A Galil DMC-4040 motion controller drives the focus and filter wheel motors. Motion commands are implemented within a custom LabVIEW application with a graphical user interface running on a linux operating system. Real-time focus and filter position information are displayed to the user and recorded for inclusion in the FITS image headers (Wells et al. 1981; Pence et al. 2010).

---

<sup>6</sup>Uniblitz is now part of Vincent Associates.

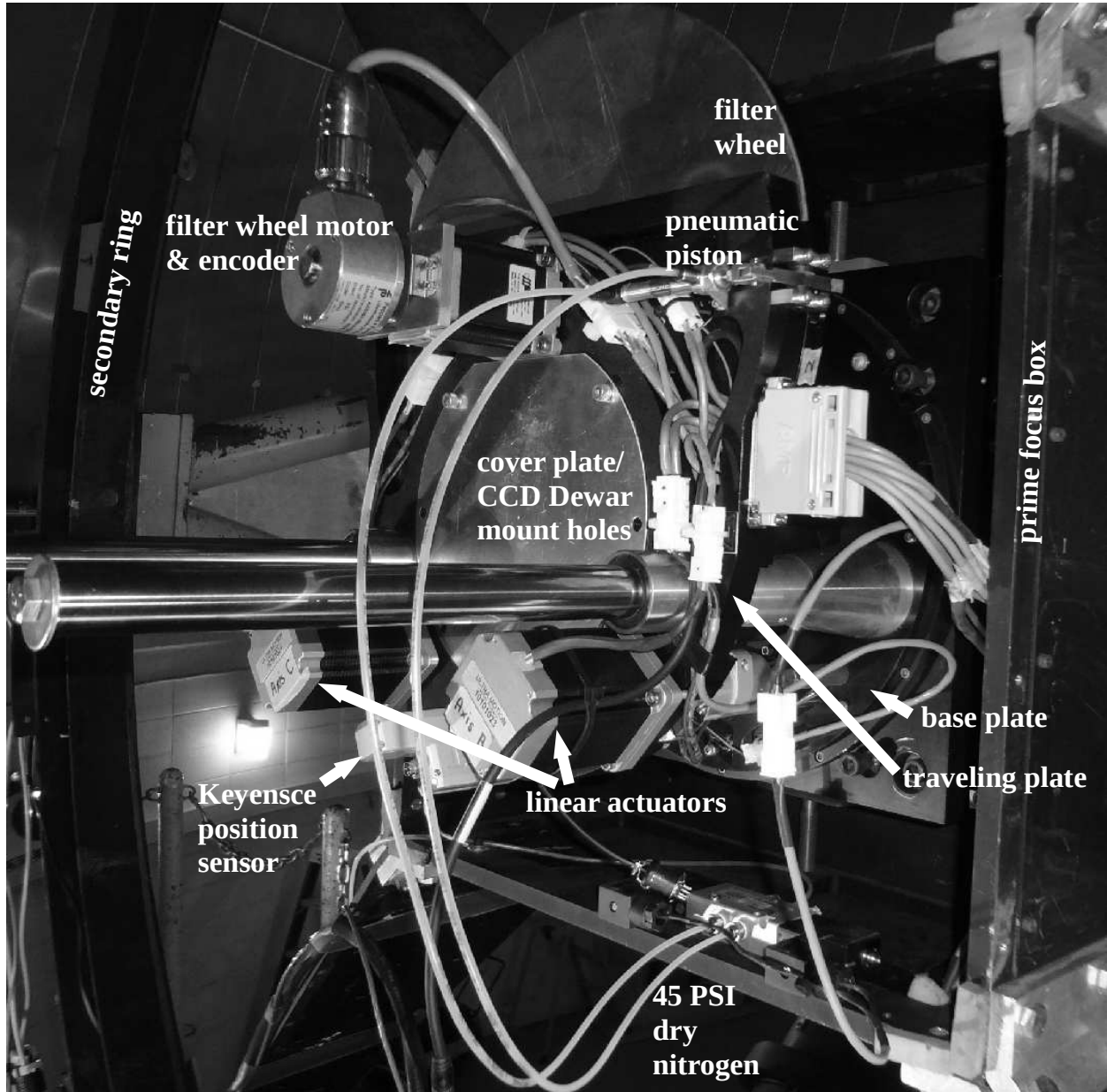


Fig. 3.— Photograph of the WIRO Double Prime instrument package on the telescope, minus the CCD Dewar, which mounts at the location of the labeled 9-inch diameter cover plate.

## 4.2. CCD Camera

The WIRO Double-Prime imaging device is a  $4096 \times 4096$  thinned back-illuminated CCD fabricated at the University of Arizona Imaging Technology Laboratory. Enhanced UV coatings optimize the quantum efficiency for the  $3600 - 4500 \text{ \AA}$  portion of the spectrum. Actual peak quantum efficiency exceeds 85% at  $3900 \text{ \AA}$  and remains above 75% through  $7000 \text{ \AA}$ . The CCD was mounted in a custom Dewar fabricated by Astronomical Research Cameras, Inc., which also supplied the readout electronics (ARC Generation III controller). The CCD window is fabricated from UV-grade fused silica to preserve high blue throughput.

## 4.3. Detector Characteristics

The detector gain was determined for the default four-amplifier readout mode from the slopes of the signal-versus-variance relations shown in Figure 4. Both quantities were measured from pairs of three-second dome flats with consecutive pairs taken at increasing dome lamp intensity levels. The results are shown by the red filled circles in Figure 4 and the best linear fits to these measurements are shown by the gray lines. To monitor the stability of the light source, pairs of exposures were interleaved by a single two-second exposure at a constant intensity level.

The plotted quantity,  $\langle S \rangle$ , is the average signal in ADU measured over each image pair in clean regions of each quadrant of the detector array. The variance,  $\sigma^2$ , was measured over identical pixel regions in the difference image between each image pair.<sup>7</sup> This process reduces the effect of pixel-to-pixel sensitivity variations in the flat field which would otherwise produce scatter in the pixel levels and would lead to a biased gain measurement. The procedure does not account for noise introduced during bias subtraction of the flat field frames, however for the low level Poisson distributed counts in bias frames these noise terms are negligible. Table 2 lists the gain measured in each quadrant from the best linear fit to the signal-to-variance relation over all 41 dome flat pairs. The random measurement errors are calculated from the scatter in the relation after iteratively re-fitting with a single data point omitted at each step. Measured gains are very near  $2.6 \text{ electrons ADU}^{-1}$  in all quadrants.

The use of three-second flats in the gain measurements was chosen to ensure dark current remained negligible throughout. To check that these short exposures do not suffer from shutter timing effects (see below), which could otherwise bias our gain measurements,

---

<sup>7</sup>Note that the plotted quantity  $\sigma^2$  is half the variance measured in a given difference image. The extra factor 0.5 accounts for the fact that the variance is doubled when subtracting two dome flat pairs.

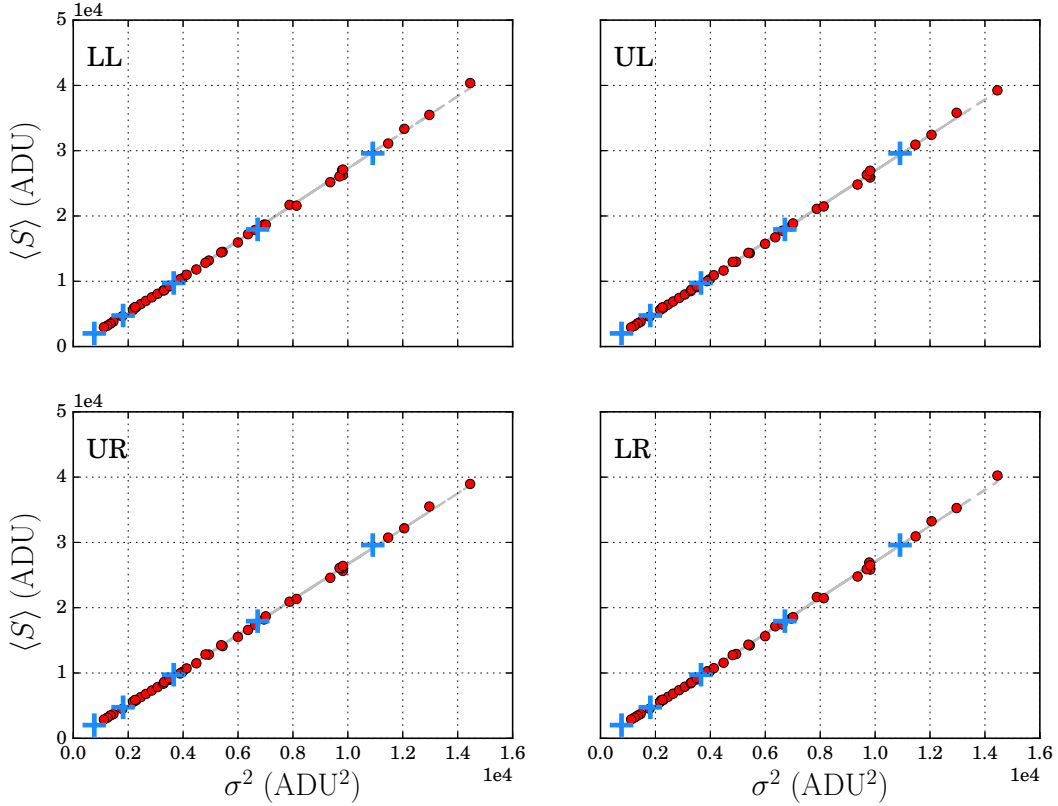


Fig. 4.— Signal-versus-variance ( $\langle S \rangle - \sigma^2$ ) plots for each of the four quadrants of the Double-Prime array. Clockwise from the top left, panels correspond to the lower-left (LL $\equiv$ north-east), upper-left (UL $\equiv$ north-west), lower-right (LR $\equiv$ south-east) and upper-right (UR $\equiv$ south-west) quadrants respectively. The signal was measured in clean regions of each quadrant over pairs of three-second dome-flats at increasing lamp intensity levels. The variance was measured in the difference images between pairs of dome flats in order to remove pixel-to-pixel variation in the flat field. The gray lines are the best fits to the red filled circles, which are the data taken from the set of three-second dome flats. The slope of the line gives the gain of the relevant CCD (see Table 2). The blue crosses show the signal and variance measured from a set of ten-second dome flats. The resulting gain measurements are entirely consistent with the results found from the three-second flats.

the procedure was repeated with a set of ten-second dome flats. The resulting measurements are overlaid in Figure 4 as blue crosses and are found to be entirely consistent with the results returned from the three-second flats.

Using the measured gain,  $G$ , the readnoise in electrons was calculated from the standard deviation in the difference images of bias frame pairs,  $\sigma_{B1-B2}$ , as  $\sigma_{RN} = G \frac{\sigma_{B1-B2}}{\sqrt{2}}$ . The readnoise calculations were performed over identical pixel areas as defined for the gain measurements, and the quantities reported in Table 2 are the median readnoise measurements over 342 unique bias frame pairs for each quadrant.

The linearity of all four quadrants has been characterized via a sequence of dome flats at constant light level exposed for durations increasing by two seconds until saturation. Each integration was followed by an exposure of two seconds in order to monitor the stability of the light source. Figure 5 illustrates the linearity curves plotted as the average count rate versus time for each CCD quadrant. Saturation occurs broadly at  $\sim 60,000$  ADU across all detectors with no measurable difference in the saturation level in each quadrant within counting errors. The blue crosses correspond to the count rate measured in five smaller regions sampling the corners and center of each quadrant. The five data points at each interval are largely indistinguishable on the plot scale and there is no indication of a measurable variation in the saturation level across each detector within counting errors. The dashed gray line is a linear fit with forced zero slope to the data between  $t_{\text{exp}} = (4 - 14)$  s. There is an obvious deviation from the fit at  $t_{\text{exp}} = 2$  s. Although we do not rule out the possibility of non-linearity at low signal levels the more likely origin of this effect is the finite shutter open/close timing, which will alter both the true exposure time and the illumination pattern across the array when the duration of the exposure is comparable to the shutter timing.

The effects of shutter timing on illumination have been investigated using a series of

Table 2. WIRO Double Prime Gain and Readnoise

Detector	Gain ( $e^-/\text{ADU}$ )	Readnoise (ADU)
LL (NE)	$2.677 \pm 0.003$	$5.41 \pm 0.16$
UL (NW)	$2.639 \pm 0.003$	$5.17 \pm 0.21$
UR (SW)	$2.619 \pm 0.003$	$5.20 \pm 0.21$
LR (SE)	$2.664 \pm 0.004$	$5.19 \pm 0.21$

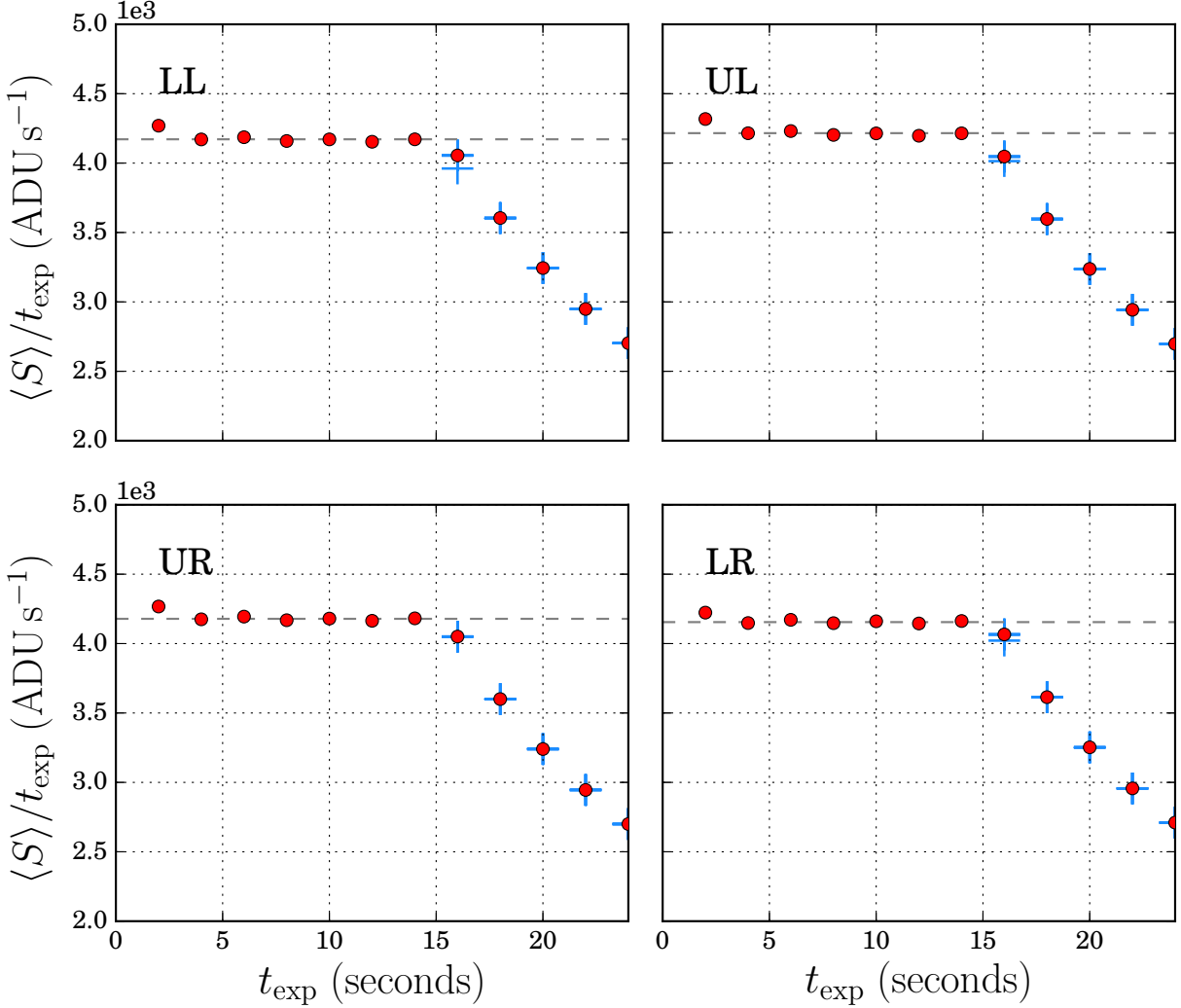


Fig. 5.— Linearity curves for each of the four Double-Prime array quadrants. Clockwise from the top left, panels correspond to the lower-left (LL $\equiv$ north-east), upper-left (UL $\equiv$ north-west), lower-right (LR $\equiv$ south-east) and upper-right (UR $\equiv$ south-west) quadrants respectively. Signal was measured in a series of dome flats at constant intensity with exposure times increasing in two-second intervals until saturation. Filled circles give the average count rate in units of  $\text{ADU s}^{-1}$ . Five crosses at each interval beyond saturation give the average count rate in small regions sampling the corners and center of each CCD. At each interval crosses are largely indistinguishable from one another on the plot scale. Each detector saturates at  $\sim 60000$  ADU and there is no measurable difference in the saturation level between CCDs or within any single CCD within counting errors. The dashed gray line shows a linear fit with forced zero slope to data points between  $t_{\text{exp}} = (4 - 14)$  s. The deviation to the fit at  $t_{\text{exp}} = 2$  s is likely attributable to shutter timing effects.

dome flats taken at constant light levels for exposure times varying between 0.1 and four seconds. Figure 6 shows the ratio of a sample of these dome flats to an 8 second dome flat after normalizing by exposure time. The legends in each panel give the exposure time of the comparison image in the top left and the standard deviation of the flat ratio in the bottom left. Illumination clearly varies across the detector arrays at short exposure times, with the edges of the fields most affected. As the exposure time increases the effect becomes less pronounced until the illumination across a two-second flat-field becomes indistinguishable from that across an eight-second flat-field. Due to the effects identified in Figures 5 and 6, exposure times of less than four seconds are not recommended.

#### 4.4. Image Quality

WIRO Double-Prime has a field of view of approximately  $39'$  at a nominal on-axis scale of  $0.58'' \text{ pix}^{-1}$ . For comparison, the full moon subtends an average angle of  $31'$  on the sky. Figure 7 shows a false-color image of M31, produced from a combination of three 60 s exposures in the  $u'/g'/r'$  filters, represented as blue/green/red.<sup>8</sup> The instrument suffers from a small amount of pincushion distortion, which is inherent in the design of the four-element prime-focus corrector. The nominal plate scale at the center of the field is  $0''.581 \text{ pix}^{-1}$  but drops to near  $0''.566 \text{ pix}^{-1}$  near the corners of the usable field ( $27'$  field angles). A geometrical transformation (such as the *IRAF* `geotran` task, or similar), determined by mapping a bright star across a regular grid pattern, is used to correct the images to a uniform plate scale of  $0''.58 \text{ pix}^{-1}$  prior to co-adding dithered images or performing other high-level processing steps.

#### 4.5. Filter Set, Sensitivity & Color terms

Under normal operation the filter wheel houses five Astrodon manufactured SDSS-like filters (Doi et al. 2010) denoted  $u', g', r', i', z'$ . Figure 8 plots the measured filter curves for  $u', g', r'$  and  $i'$ .<sup>9</sup> The manufacturer’s archetype filter curves are plotted in gray and differ from the true curves by no more than a few percent. Also plotted in Figure 8 is the average detector quantum efficiency curve (provided courtesy of R. Leach).

---

<sup>8</sup>Some residual off-axis aberrations can be seen at large field angles as a result of non-optimal corrector alignment that is still being diagnosed as of this writing.

<sup>9</sup>The  $z'$  band filter curve has not been accurately measured by the authors at the time of writing.

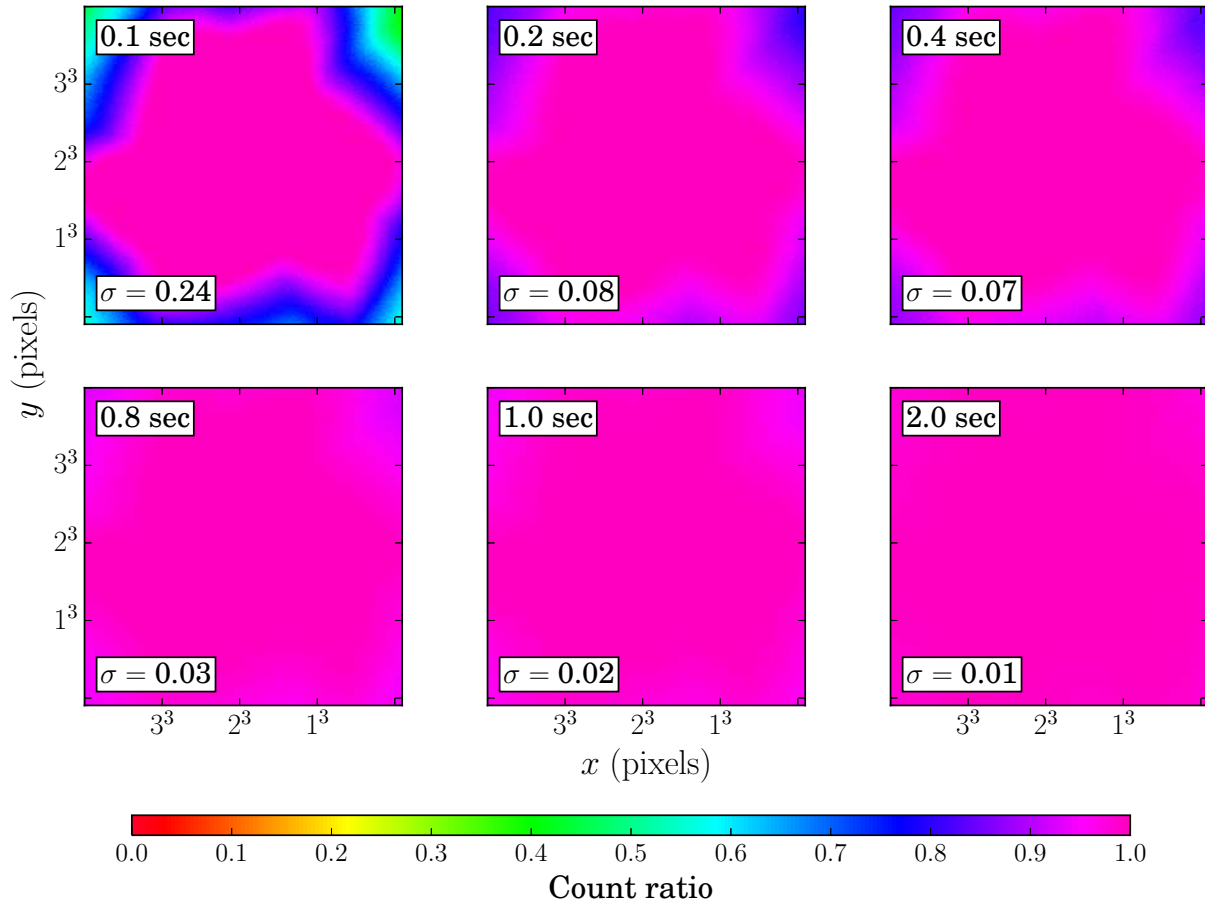


Fig. 6.— Shutter timing effects shown as the ratio of a series of dome flats to a reference eight-second dome flat at a constant light intensity level. Plot legends give exposure times in the top left corners and standard deviations in the bottom left corners for the relevant flat ratio in the series. Non-uniform illumination of the array is clear during the shortest exposure times but undetectable in the two-second flat.



Fig. 7.— A  $u'/g'/r'$  image of M31, illustrating the nearly  $40'$  field of view.

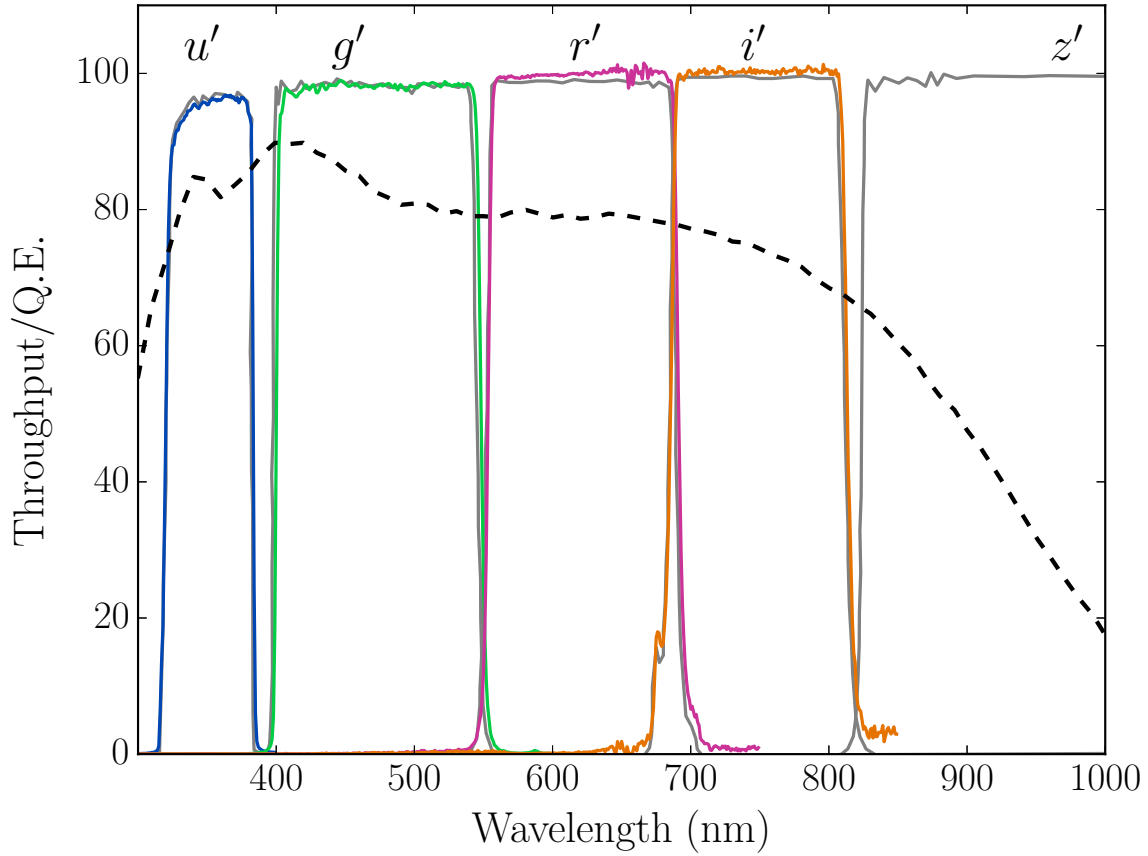


Fig. 8.— The measured throughput of the Astrodon  $u'$ ,  $g'$ ,  $r'$ , and  $i'$  filters (colored curves). The  $z'$  band filter curve has not been accurately measured by the authors at the time of writing. Gray curves show the manufacturer archetype filter curves, which differ from the true filter curves by no more than a few per cent. The black curve shows the average quantum efficiency of the Double-Prime  $4096^2$  array.

Ideally one would like to characterize the sensitivity of the telescope and optical system by tying Double-Prime imaging data to the “natural magnitude system” defined by wavelength-dependent quantities such as the photon weighted central wavelengths of each filter, the quantum efficiency of the CCD array, the mirror reflectivity and the characteristic atmospheric absorption at Mt. Jelm. Since the total system throughput is not well known we instead characterize the sensitivity of the telescope with respect to the SDSS magnitude system.

SDSS photometry is intended to be on the AB system (Oke & Gunn 1983), however small offsets from the AB standard are known to exist (Smith et al. 2002). Nevertheless the wide use of the SDSS system throughout astronomy and the close relationship between the SDSS and Double Prime filter sets (see below) make it a good choice on which to base the following analysis.

The system sensitivity has been characterized from a single night’s observations of a field at R.A.=2 hrs, Dec.=+1°(within the SDSS Stripe 82 region (Annis et al. 2014)) at airmasses ranging from between 1.27 to 2.5. The data were taken in photometric conditions during which the average measured extinction was  $\kappa(u', g', r', i', z') = (0.47, 0.17, 0.09, 0.07, 0.06)$  mag airmass<sup>-1</sup>. The Double-Prime zero points for the night are given in Table 3 as the average difference between the measured stellar instrumental magnitudes and the SDSS magnitudes over the target field linearly extrapolated to zero airmass. It should be stressed that even in photometric conditions zero points will vary on a nightly basis due to changing atmospheric conditions and over longer time scales due to wide ranging factors such as degradation of the mirror coating or the anti-reflection coatings on optical elements. Therefore these results should serve as a guide only, useful for comparisons with other telescopes or for approximate “on the mountain” photometry.

Table 3. WIRO Double Prime Zero Points

Band	Z.P. (mag.)
$u'$ (Astrodon)	$24.52 \pm 0.03$
$g'$ (Astrodon)	$25.31 \pm 0.02$
$r'$ (Astrodon)	$24.90 \pm 0.02$
$i'$ (Astrodon)	$24.37 \pm 0.02$
$z'$ (Astrodon)	$23.74 \pm 0.03$

In Figure 9 we compare the measured Double Prime and SDSS archive colors of stars in the target field to define color transformations between the two systems. We plot SDSS PSF magnitudes versus Double Prime aperture magnitudes measured in a wide 16-pixel radius aperture to reduce the need for significant aperture corrections, which can be difficult to determine due to image deformation at the field edges (see section 4.4). From top to bottom Figure 9 plots  $u - u' : u' - g'$ ,  $g - g' : g' - r'$ ,  $r - r' : r' - i'$ ,  $i - i' : r' - i'$  and  $z - z' : i' - z'$ . In each panel the best fitting linear color relation is shown as a dashed line. The fit was made to all objects in the field with magnitude errors  $\delta(m) < 0.05$  after iteratively clipping  $3\sigma$  outliers. It is clear from the plot that the color terms in each case are small. In comparison to the SDSS filters, the Astrodon filters have broadly similar central wavelengths but their overall shapes are more top-hat like. The Astrodon  $r'$  band is slightly broader than the corresponding SDSS band while the SDSS  $g$  and  $i$  bands are shifted slightly to the blue and red respectively compared to  $g'$  and  $i'$ . These differences likely account for the comparatively larger color terms in these bands. The best fit color relations are defined as follows;

$$\begin{aligned}
 u &= u' - 0.008(u' - g') \\
 g &= g' + 0.039(g' - r') \\
 r &= r' - 0.031(r' - i') \\
 i &= i' - 0.086(r' - i') \\
 z &= z' + 0.004(i' - z')
 \end{aligned}
 \tag{1}$$

## 5. Remote Operation at WIRO

### 5.1. Infrastructure for Fully Remote Operation

Good astronomical observing sites are invariably remote and can present significant challenges to observatory operations and users alike. Since the arrival of high-bandwidth low latency networking in the mid 1990s professional observatories have realized the increase in efficiency, cost effectiveness and safety offered through remote operations. Observatories can now be minimally staffed, users do not need to travel long distances, coordination of food and water supplies are less complex, operations can continue during periods of hazardous weather, etc. Consequently most professional observatories now offer full telescope and instrument control from somewhere other than a mountain top.

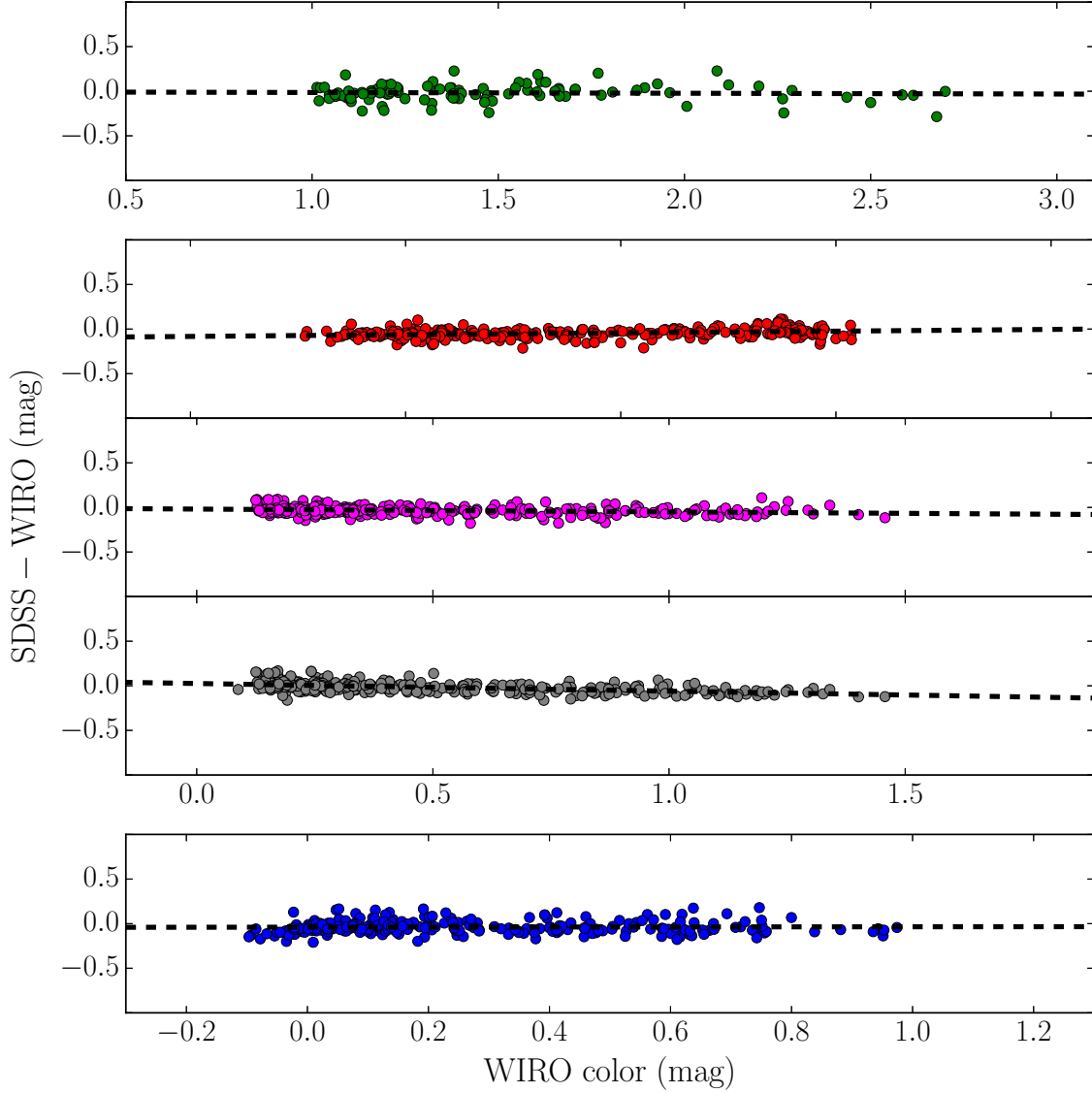


Fig. 9.— Color relationships between WIRO Double Prime and SDSS imaging in the Astrodon ( $u'$ ,  $g'$ ,  $r'$ ,  $i'$ ,  $z'$ ) and standard SDSS ( $u$ ,  $g$ ,  $r$ ,  $i$ ,  $z$ ) filter sets. Top to bottom shows  $u - u' : u' - g'$ ,  $g - g' : g' - r'$ ,  $r - r' : r' - i'$ ,  $i - i' : r' - i'$ ,  $z - z' : i' - z'$ . The dashed lines show the best fit to the main distribution of stellar colors plotted as filled circles. The best fit color relations are given by equation set 1.

The 10 m Keck telescopes have offered remote operations for many of their instruments from their headquarters in Waimea since 1996 and from the United States mainland since 1998 (Wirth et al. 2008). Keck has shown that solutions can be both adaptable and scalable by serving facilities with similar instrument control interface designs such as those at the UCO/Lick Observatory including the 1 m Nickel (Grigsby et al. 2008). Other professional class optical and near infrared telescopes providing detailed literature on their remote capabilities include Subaru (Kosugi et al. 2004), the Canada-France-Hawaii Telescope (CFHT; Vermeulen et al. 2014), the NASA Infrared Telescope Facility (IRTF) (Bus et al. 2002) and the Southern Astrophysical Research Telescope (SOAR; Cecil et al. 2002).

As networking and remote control technology has progressed, the technical infrastructure costs have fallen, allowing University owned observatories to take on similar projects with small telescopes. As well as enjoying the benefits of increased operational efficiency these smaller observatories are often able to increase student collaboration and training. Recent examples include the Antarctic Bright Star Survey Telescope (BSST; Zhang 2016), the Lee Sang Gak Telescope (LSGT; Im et al. 2015) and the Lowell Observatory 0.8 m Telescope (Bui 2010).

In realizing the fully remote operation of WIRO the authors undertook a slightly different challenge; WIRO is neither a large national facility nor a small educational project. WIRO has power, logistical and operational demands that are comparable to a small national facility but has just two dedicated full time staff. Since its construction WIRO has been operated in the traditional manner, requiring at least two on-site observers as a matter of safety in light of its remote location. Students and faculty serve as the instrument scientist, telescope operator, and observer, given that there are no nighttime staff. In 2010 we committed to a series of infrastructure upgrades to enable single-user operation from the safety and convenience of the UW campus. Fully remote operation required installation of reliable backup power, reliable high-bandwidth communications, and a series of modifications to observatory infrastructure to enable remote operation of electrical circuits and key facility mechanisms used during nightly observing.

A CumminsOnan Model 60DSFAD diesel autostart generator rated to 55 kW at 9000 feet elevation was installed in the fall of 2013, replacing the obsolete 1970's-era 8 kW generator. Failure of line power triggers automatic activation of the generator and the Cummins model OTCB transfer switches that disconnect line power and enables the generator feed. A delay of two minutes is imposed to prevent unnecessary generator wear during momentary power events. The generator is housed in a heated ( $\gtrsim 3^{\circ}$  C) machine shed attached to the northeast exterior wall of the dome. The 140 gallon diesel fuel tank is capable of supplying power sufficient for all observatory functions for up to seven days.

Critical observatory functions are powered by a 10 kVA uninterruptible power supply (UPS) with a runtime of  $\sim 12$  minutes at nominal nighttime observing loads. A network interface within the UPS is configured to notify staff via email or text upon power outages or critical events. UPS-powered items include the telescope drive motors and control system, dome shutters, mirror covers, dome video cameras, network infrastructure, telescope control computer, and data acquisition computers. The nominal run time at full load is sufficient to allow startup of the diesel generator or, failing that, safe shutdown of the observatory.

Observatory control communications occur over ethernet using a dedicated local area network (LAN) at WIRO anchored by a 48-port network switch. A pair of Motorola PTP800 transceivers and 2' diameter antennas provides a 25-mile line-of-sight link between WIRO and the UW campus network. Radios at each end of the link have their independent battery backup with a 12-hour runtime. The licensed 11 GHz channel provides throughput of 300 megabits  $s^{-1}$ , sufficient for routine operation that requires remote displays (via Vncviewer remote desktop) of WIRO computer desktops, streaming video from dome cameras, monitoring of critical observatory functions, and periodic transfer of astronomical images (32 MB per exposure).

Figure 10 provides a schematic of the observatory power distribution and communications. Heavy dotted lines indicate 120 V power, thin dotted lines indicate control-voltage connections, and solid thin lines show TCP/IP connections on the local area network (LAN). Figure 10 illustrates the layout of key observatory infrastructure but is not exhaustive; multiple electrical circuits have been grouped into single logical blocks for simplicity of presentation. Power to each of the key observatory devices is controlled by a bank of Functional Devices, Inc. Relay-in-a-Box (RIB) relays controlled using a National Instruments compactRIO (cRIO-9074) controller. A custom LabVIEW graphical user Observatory Control (OC) interface written by the UW Division of Research Support allows a remote user to monitor and control each relay. The OC GUI allows activation of the dome shutters, mirror covers, dome lights, dome fan, along with all critical facility electrical circuits. The relays can also be controlled locally through the use of a manual override switch that bypasses the cRIO controller. The OC GUI displays realtime status on battery runtime (via TCP link to the UPS), weather (via TCP link to the WIRO Davis Vantage Pro weather station), and humidity/wetness (via an RS232 to optical fiber connection that provides electrical isolation). The OC GUI may be run either locally on observatory computers or from the UW campus remote observing computer. An Aurora Eurotech Cloud Sensor III cloud/wetness sensor mounted on the roof triggers (via the cRIO) a dome closure if precipitation is detected. As an additional safety precaution, the telescope control loop code includes a thread that monitors the network connection to the remote computer on campus; it closes the dome and stows the telescope in the event of a network failure.



Lightning protection at the observatory is provided site-wide by MCG Surge Protection devices and a building-wide web of metal cable grounded to large copper plates underneath the mountaintop. The local area network ethernet switch and all ethernet devices are protected by an AC Systems 48-port POE surge protection device that helps eliminate damage from lightning-induced surges that have historically occurred. Additional surge suppression is installed on the RS232 and low-voltage analog signal conductors leading from the dome motors and encoders to the GD control system electronics; because of their length, these are historically susceptible to lightning-induced surges.

## 5.2. Procedures for Fully Remote Operation

Remote operation requires that an observer on the UW campus monitor observatory weather, observatory status, and instrument status in real time. The WIRO Davis Vantage Pro weather station provides real time temperature, humidity, wind speed and wind direction information to the OC GUI. An observer is required to close the dome if sustained wind speeds surpass 30 mph and the wetness sensor triggers dome closure if humidity exceeds 80%. One AXIS Q6032-E network camera<sup>10</sup> in a heated enclosure mounted on the roof of the living quarters allows a 360-degree view of the mountain top, dome exterior, cloud conditions, and weather, even in low-light conditions. Figure 11 shows an average of three 0.5 s exposures from the roof camera facing east during New Moon. The lights of Laramie, WY, are clearly visible at far left, along with a thin cloud band illuminated by the lights from Cheyenne, WY 60 miles to the east. The image captures the rising constellations Gemini and Orion. The image has been cropped by about 10% and 30% in the horizontal and vertical directions, respectively, but still serves to illustrate the  $>2^\circ$  field of view. Two additional AXIS Q6032-E network cameras are mounted on opposite sides of the dome interior, allowing full pan/tilt/zoom imaging of any portion of the telescope and dome. These cameras are used during startup and shutdown sequences to visually verify correct operation of mirror covers, dome shutters, and other key mechanisms. An AXIS P8221 audio module inside the dome provides audio feedback to a remote observer.

## 6. Summary

In the dawning era of time-domain astronomy, WIRO is positioned to make outsized returns as one of the largest observatories operated by a single institution.

---

<sup>10</sup>This product has been discontinued, contact AXIS Communications to identify an equivalent.

The ability to implement flexible schedules or assign large blocks of time (even hundreds of nights!) to a single program will allow the upgraded Wyoming Infrared Observatory to participate in campaigns of arbitrary cadence and duration. Future instrument and telescope upgrades will permit visiting Cassegrain instruments a more favorable beam once a new wide-field f/9 secondary is constructed. As historically has been the case, one of the strengths of the Observatory will continue to be student training. Graduate and undergraduate students, along with visiting teams from other institutions, will obtain hands-on experience in telescope operation, programming, digital data analysis, optics, instrument design, electronics, and real-time remote operation of a major scientific facility.

This work was made possible by NASA through EPSCOR grant NNX10AM10H, and the National Science Foundation through grants AST 0307778 and AST/PREST 0721281. We are grateful to Charles Harmer for his assistance with the design of the prime-focus corrector. We thank Bob Berrington and Andy Monson for assistance with the installation of the prime focus corrector. We thank the Lander, WY high school astronomy club, and their instructor, Joe Meyer, for inspiration to make WIRO a vehicle for learning and outreach for students of all ages. We thank Robert Gehrz, John Hackwell, the State of Wyoming, and the National Science Foundation for the vision to construct WIRO 40 years ago. Finally we would like to thank the anonymous referee for their work in helping to improve this paper.

## REFERENCES

- Annis, J., Soares-Santos, M., Strauss, M. A., et al. 2014, *ApJ*, 794, 120
- Buie, M. W., 2010 *Advances in Astronomy*, 130172, 12 Strauss, M. A., et al. 2014, *ApJ*, 794, 120
- Bus, S. J., Denault, A. J., Rayner, J. T., et al., 2002 *Proc. SPIE*, 4845, 94
- Cecil, G. N., Crain, A. & Schumacher G., et al., 2002 *Proc. SPIE*, 4845, 72
- Dale, D. A., Barlow, R. J., Cohen, S. A., et al. 2010, *ApJ*, 712, L189
- Doi, M., Tanaka, M., Fukugita, M., et al. 2010, *AJ*, 139, 1628
- Gehrz, R. D., & Hackwell, J. A. 1978, *S&T*, 55, 466
- Gehrz, R. D., Hackwell, J. A., Grasdalen, G. I., et al. 1980, *ApJ*, 239, 570
- Gehrz, R. D., Grasdalen, G. L., Castelaz, M., et al. 1982, *ApJ*, 254, 550

- Hackwell, J. A., Gehrz, R. D., & Grasdalen, G. L. 1979, ApJ, 234, 133
- Hackwell, J. A., Grasdalen, G. L., & Gehrz, R. D. 1982, ApJ, 252, 250
- Grigsby, B., Chloros, K., Gates, J., et al., 2008, Proc. SPIE, 7016, 701627
- Im, M., Choi, C. & Kim, K., 2015, Journal of Korean Astronomical Society, 48, 207
- Kobulnicky, H. A., Kiminki, D. C., Lundquist, M. J., et al. 2014, ApJS, 213, 34
- Kosugi, G., Sasaki, T., Yagi, M., et al., 2004 Proc. SPIE, 5496, 695
- Oke, J. B. & Gunn, J. E. 1983, ApJ, 266, 173
- Pence, W. D., Chiappetti, L., Page, C. G., et al. 2010 A&A, 524 A42
- Smith, J. A., Tucker, D. L., Kent, S., et al. 2002 AJ, 123, 2121
- Spillar, E. J., Dumbrill, D., Grasdalen, G. L., et al. 1993 PASP, 105, 6165
- Vermeulen, T., Thomas, J. & Burdullis, T., et. al 2014 ASPC, 485, 53
- Wells, D. C., Greisen, E. W., Harten, R. H., 1981 A&AS, 44, 363
- Wirth, C. G., Kibrick, R. I., Goodrich, R. W., et al. 2008 Proc. SPIE, 7016, 70160Y
- Wynne, C. G. 1973, MNRAS, 165, 1P
- Wynne, C. G. 1965, Appl. Opt., 4, 1185
- Zhang, G.-y., Wang, J., Tang, P.-y., et al. 2016 MNRAS, 455, 1654

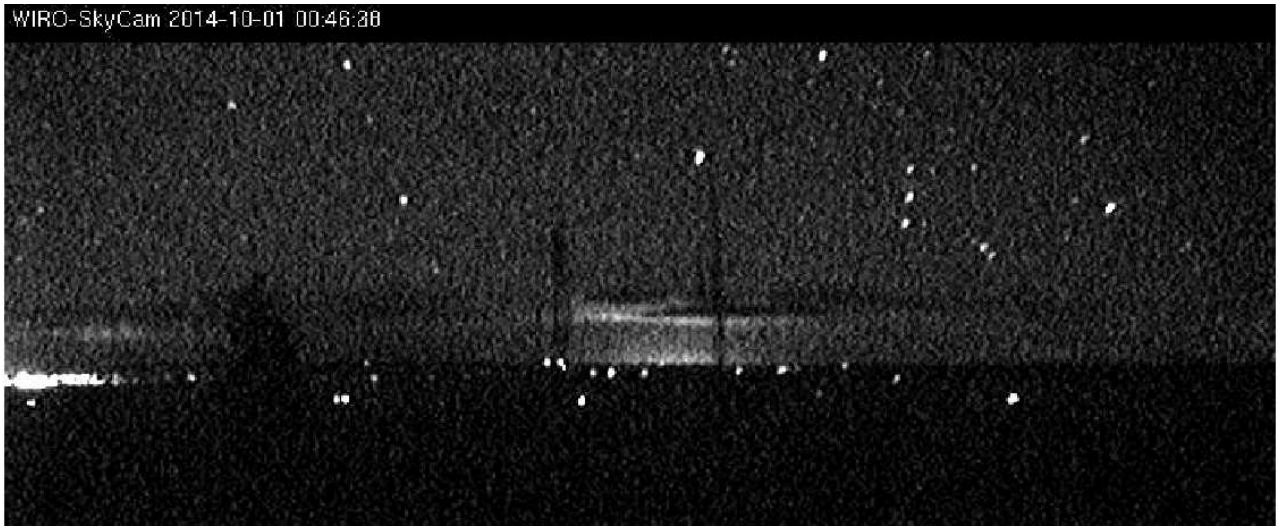


Fig. 11.— An average of three 0.5 s exposures (slightly cropped in the horizontal and vertical directions) from the WIRO roof camera looking east during new moon. The lights of Laramie, WY, (far left) a thin cloud band illuminated by the lights of Cheyenne, WY (center), and the rising constellations Gemini and Orion are visible.